

Optical appearance of a thin-shell wormhole with a Hayward profile

Sen Guo^{1,a}, Guan-Ru Li^{1,b}, En-Wei Liang^{1,c}

¹ Guangxi Key Laboratory for Relativistic Astrophysics, School of Physical Science and Technology, Guangxi University, Nanning 530004, People's Republic of China

Received: date / Accepted: date

Abstract The optical properties of a thin-shell wormhole (TSW) with a Hayward profile is investigated. Adopting the ray-tracing method, we demonstrate that the TSW's contralateral spacetime is capable of reflecting a significant portion of light back to the observer spacetime. We analyze the effective potential, light deflection, and azimuthal angle of the TSW and find that these quantities are affected by the mass ratio of the black holes (BHs). Specifically, if the mass of the contralateral spacetime BH is greater than that of the original spacetime BH, and the impact parameter satisfies the condition $Hb_{c2} < b_1 < b_{c1}$, the trajectory of the photon exhibits round-trip characteristics. Assuming the presence of a thin accretion disk surrounding the observing spacetime BH, our results indicate that the image formed by the TSW exhibits additional photon rings and a lensing band compared to an image produced by a BH alone.

1 Introduction

Black holes (BHs) are intriguing astronomical objects whose existence is predicted by the theory of general relativity (GR). One of their most captivating characteristics is their ability to cause gravitational lensing of light. Since photons follow the null geodesics of the spacetime metric, studying the geodesic equation provides valuable insights into the bending of light. In an attempt to describe the deflection of light around a BH using the concept of a BH shadow, Sygne determined that the shape of a spherical BH (Schwarzschild BH) shadow is a perfect circle [1]. Building upon the Schwarzschild BH model, Bardeen proposed that the deformation of the BH shadow is related to the BH's angular momentum [2], specifically in the context of rotating

BHs (Kerr BHs). Extensive research has been conducted to investigate the geometry of BH shadows in various modified gravity contexts were also discussed in the existing literatures [3–24].

In astrophysical observations, it is common to find a luminous accretion disk surrounding a BH. Luminet demonstrated that the presence of the BH shadow and ring depends on the position of the accretion disk [25]. Investigating a scenario with a spherical accretion disk, Narayan *et al.* studied the optical appearance of a Schwarzschild BH and showed that the size of the BH shadow remains unaffected by the radius of the spherical accretion disk [26]. When considering a thin accretion disk surrounding the Schwarzschild BH, Gralla *et al.* presented an elegant description of the BH shadow, lensing ring, and photon ring [27]. They discovered that the brightness of the shadow exhibits a logarithmic divergence at the photon ring and that the details of the accretion affect the BH shadow. The impact of the location and morphology of the accretion flow surrounding the BH spacetime has been extensively investigated in various modified gravity theories [28–38].

By employing numerical simulations and ray-tracing techniques, Falcke *et al.* demonstrated the feasibility of observing the BH shadow [39]. The Event Horizon Telescope (EHT) collaboration achieved a breakthrough by obtaining the first-ever image of the supermassive BH located at the center of the elliptical galaxy Messier 87* (M87*) [40–45]. This image revealed a prominent ring-shaped structure surrounding the BH shadow. EHT recently captured horizon-scale radio observations of Sagittarius A* (Sgr A*), the supermassive BH in our own Milky Way. The measured size of the ring in Sgr A* aligns with the predicted critical curve of the BH shadow within a 10% margin of error, providing compelling evidence for GR in the regime of strong gravitational fields [46–51]. These remarkable findings underscore the valuable insights the BH shadow offers regarding

^ae-mail: sguophys@126.com

^b2007301068@st.gxu.edu.cn

^cCorresponding author, e-mail: lew@gxu.edu.cn

the spacetime properties near the BH, establishing it as a direct and powerful experimental confirmation of GR in the realm of strong gravity [52–54].

The groundbreaking results obtained by the EHT have sparked extensive research into the optical properties of non-Kerr objects, which include BHs that deviate from the Kerr metric and horizonless ultra-compact objects [55, 56]. This research explores the characteristics of shadows cast by specific types of compact objects, such as extended Kerr BHs, additional scalar fields [57, 58], horizonless objects like boson stars [59], and wormholes [60–62]. A thin-shell wormhole (TSW) is a theoretical construct in the framework of GR that represents a “shortcut” through spacetime, connecting two distant regions. It consists of an exceedingly thin spherical shell of matter, enabling particles to pass through it and enter the “throat” of the wormhole. The shell serves as a sort of “tunnel” that allows particles to traverse vast distances in the universe without having to travel through regular space. TSWs serve as important models resembling BHs. With the exception of the innermost part, their spacetime can be identical to that anywhere in a BH. Visser proposed an effective method for describing and constructing a class of wormholes using the cut-and-paste technique [63], which involves combining two BH spacetimes. Tsukamoto investigated the gravitational lensing effect of the Schwarzschild TSW and discovered that the formation of images depends on the positions of the light source and the observer [64]. Wang *et al.* explored the influence of the unstable photon sphere on TSW and found that the TSW’s shadow size is always smaller than that of a BH [65]. Researchers examining an asymmetric Schwarzschild TSW accretion disk demonstrated that the structure of the TSW’s shadow differs from that of a BH [66]. Guerrero *et al.* argued that wormhole geometries and proposed the existence of additional light rings in the intermediate region between the critical curves of the TSW [67]. More recently, the photon-ring structure of horizonless objects characterized by two or no photon spheres has been explored [68]. The existence of multi-ring images with a non-negligible luminosity in shadow observations when one allows for the existence of other compact objects [69–73].

In contrast to irregular BHs that possess an inherent singularity at the origin of spacetime, Bardeen proposed a BH solution that is devoid of spacetime singularities [74]. Additionally, Hayward developed the regular Hayward BH solution by combining nonlinear electrodynamics with the Einstein field equations [75]. We investigated the effects of accretion flow and magnetic charge on the observable characteristics of the shadow and photon rings of the Hayward BH [76]. It is found that the geometric appearance of the Hayward BH shadow is determined by the underlying spacetime geometry, whereas the optical appearance is influenced by the properties of the accretion flow and the BH’s mag-

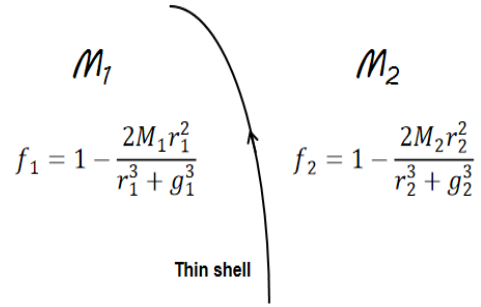


Fig. 1 A TSW with a Hayward profile serves as a mimic of a BH. The throat of the TSW establishes a connection between two distinct regions in spacetime, allowing for a light ray to pass through and link the two regions without crossing the event horizon.

netic charge.

In this analysis, we utilize the cut-and-paste technique proposed by Visser [63] to construct a TSW with a Hayward profile and investigate the optical properties of this particular class of horizonless objects. It should be noted that the construction of such a TSW involves connecting two spacetime structures with Hayward profiles. The structure of this work is organized as follows. In Section 2, we provide a brief introduction to the construction of a TSW with a Hayward profile and discuss the effective potential. Section 3 presents the analysis of light deflection in the TSW system. In Section 4, we delve into the classification of rings, transfer functions, and the corresponding optical appearance when a thin accretion disk surrounds the TSW. We draw the conclusions in Section 5.

2 Effective potential of a TSW with a Hayward profile

The Hayward BH metric can be written as [75]

$$ds^2 = -f(r)dt^2 + f(r)^{-1}dr^2 + r^2(d\theta^2 + \sin^2\theta d\phi^2), \quad (1)$$

where $f(r)$ is the metric potential,

$$f(r) = 1 - \frac{2Mr^2}{r^3 + g^3}. \quad (2)$$

The symbol M represents the mass of the BH, and g denotes the BH magnetic charge. To create a TSW with a Hayward profile, we remove the interior regions of two Hayward spacetimes and join them together at the hypersurface. The two original spacetimes are denoted as \mathcal{M}_1 and \mathcal{M}_2 , and the resulting manifold can be represented as $\mathcal{M} \equiv \mathcal{M}_1 \cup \mathcal{M}_2$. The connection between the two spacetimes forms a throat, as illustrated in Fig. 1.

Based on Eq. (1), the two spherically symmetric metrics are connected by the throat, we have

$$ds_1^2 = -f_1(r_1)dt_1^2 + f_1(r_1)^{-1}dr_1^2 + r_1^2(d\theta_1^2 + \sin^2\theta_1 d\phi_1^2), \quad (3)$$

where $i = 1, 2$ represent two spacetimes \mathcal{M}_1 and \mathcal{M}_2 . The $f_i(r_i)$ is

$$f_i(r_i) = 1 - \frac{2M_i r_i^2}{r_i^3 + g_i^3}, \quad r \geq R, \quad (4)$$

where R denote the throat radius, satisfying $R > \max\{r_{+1}, r_{+2}\}$ (r_{+} is the event horizon radius). When the magnetic charge is zero in both spacetimes, the throat connects two Schwarzschild spacetimes. If the magnetic charge is zero in one of the spacetime, the throat connects a Schwarzschild spacetime with a Hayward spacetime. If the magnetic is non-zero charge in both spacetimes, the throat connects two Hayward spacetimes.

To investigate the deflection of light in a TSW with a Hayward profile, we derive the effective potential governing its motion. We focus on photons that move exclusively on the equatorial plane. Assuming that the interaction between the photon and the throat is solely influenced by gravity, the 4-momentum of the photon remains invariant when crossing the throat. Considering the TSW definition, which ensures the continuity of the metric in the spacetime \mathcal{M} , i.e., $g_{\mu\nu}^{\mathcal{M}_1}(R) = g_{\mu\nu}^{\mathcal{M}_2}(R)$ [65], we can express the motion equation of the null geodesic as follows:

$$\frac{p_{\tilde{t}_i}^2}{f_i(r_i)} - \frac{p_{\phi_i}^2}{r_i^2} = \frac{(p_{\tilde{t}_i}^{r_i})^2}{f_i(r_i)}, \quad (5)$$

where $p^\mu = dx^\mu/d\lambda$ represents the 4-momentum of the photon, λ is an affine parameter. $p_{\tilde{t}_i}$ and p_{ϕ_i} denote the energy ($p_{\tilde{t}_i} = -E_i$) and angular momentum ($p_{\phi_i} = L_i$) of the photon, respectively, which remain constant along the geodesic due to the Killing symmetries of spacetime. By utilizing Eq. (5), we can express the radial component of the null geodesic as follow:

$$p_{\tilde{t}_i}^{r_i} = \pm E_i \sqrt{1 - \frac{b_i^2}{r_i^2} f_i(r_i)}, \quad (6)$$

where b is the impact parameter, defining as $b \equiv p_{\phi_i}/p_{\tilde{t}_i} = |L|/E$. From Eq. (6), the effective potential V_{eff} of a TSW with a Hayward profile is obtained, i.e.,

$$V_{\text{eff}_i} = \frac{f_i(r_i)}{r_i^2} = \frac{1}{r_i^2} \left(1 - \frac{2M_i r_i^2}{r_i^3 + g_i^3} \right). \quad (7)$$

The photon ring orbit satisfies the effective potential critical conditions

$$V_{\text{eff}_i}(r_{\text{ph}_i}) = \frac{1}{b_{c_i}^2}, \quad V'_{\text{eff}_i}(r_{\text{ph}_i}) = 0, \quad (8)$$

in which r_{ph} denotes the radius of the photon ring, and b_c represents the critical impact parameter. Table. 1 presents the values of critical impact parameters for a TSW with a Hayward profile at various magnetic charges. The findings

b_{c_i}/g	0	0.2	0.4	0.6	0.8
b_{c_1}	5.19615	5.19461	5.18373	5.15336	5.09013
b_{c_2}	6.23538	6.23431	6.22679	6.20603	6.16412

Table 1 The critical impact parameters for a TSW with a Hayward profile, considering different magnetic charges. The BH masses are set as $M_1 = 1$ and $M_2 = 1.2$, while the magnetic charge is varied as $g = 0, 0.2, 0.4, 0.6, 0.8$.

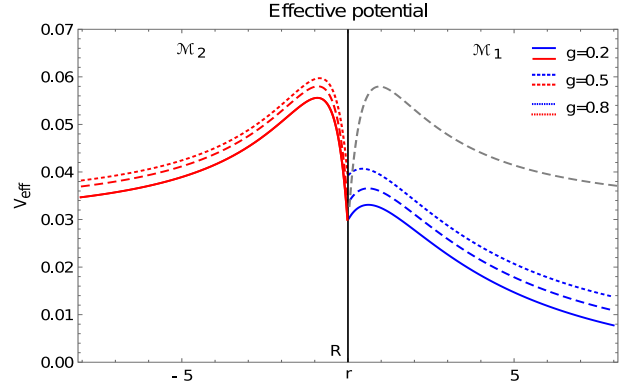


Fig. 2 The effective potential of a TSW with a Hayward profile as a function of radius for different magnetic charge. The blue and red curves two Hayward spacetimes with BH masses $M_1 = 1$ and $M_2 = 1.2$, respectively. The throat radius is chosen as $R = 2.6$. The gray curve represents the effective potential function with the same spacetime parameters, namely $M_1 = M_2 = 1.2$ and $g_1 = g_2 = 0.5$.

reveal that as the magnetic charge (g) increases, the critical impact parameter (b_{c_i}) decreases. This indicates that the presence of a higher magnetic charge causes the photon ring to be pushed inward towards the BH, resulting in a smaller critical impact parameter.

Figure 2 depicts the effective potential of a TSW with a Hayward profile as a function of radius, revealing notable difference compared to the case of a Hayward BH. The throat of the TSW connects two distinct spacetimes, denoted as \mathcal{M}_1 and \mathcal{M}_2 . When the masses satisfy $M_1 = M_2$, the effective potential functions are identical on both sides of the throat, indicating consistency in the critical curves of the two spacetimes. However, if $M_1 < M_2$, although the effective potential is equal at the throat, the highest point of the effective potential curve in spacetime \mathcal{M}_2 exceeds that in \mathcal{M}_1 . This implies that the effective potential in spacetime \mathcal{M}_2 can reflect some light from spacetime \mathcal{M}_1 . Furthermore, we observe that a larger magnetic charge leads to a more pronounced peak in the effective potential, which is consistent with the behavior observed in the case of the Hayward BH.

3 Light trajectory and deflection angle of a TSW with a Hayward profile

The phenomenon of light deflection in a BH can be categorized into three distinct situations. Firstly, when the

impact parameter (b) is greater than the critical impact parameter (b_c), the gravitational force causes the light ray to be deflected towards the observer. Secondly, when b is smaller than b_c , the light ray enters the BH and ultimately falls into the singularity. Lastly, when b is equal to b_c , the light ray orbits multiple times along the photon orbit of the BH, resulting in the formation of a luminous ring [27]. However, the behavior of photons in a TSW differs significantly from that in a BH. Consequently, a reevaluation of light deflection is necessary in the analysis of TSW.

Let's assume that light enters the spacetime \mathcal{M}_1 from infinity with an impact parameter of b_1 . The deflection of light can be classified into three different scenarios depending on the mass relationship between the two spacetimes:

- *Case 1* $M_1 = M_2$: The critical impact parameter satisfies $b_{c_1} = b_{c_2}$. The light passes through the throat into the spacetime \mathcal{M}_2 within the necessary condition $b_1 < b_{c_1}$, and then returns to the spacetime \mathcal{M}_1 .
- *Case 2* $M_1 > M_2$: The critical impact parameter satisfies $b_{c_1} > b_{c_2}$. If $b_1 < b_{c_2}$, the light passes through the throat into the spacetime \mathcal{M}_2 , and then returns to the spacetime \mathcal{M}_1 . If $b_1 = b_{c_2}$, the light will provide additional brightness for the BH photon ring in the spacetime \mathcal{M}_2 . If $b_1 > b_{c_2}$, the light goes to infinity in the spacetime \mathcal{M}_2 .
- *Case 3* $M_1 < M_2$: The critical impact parameter satisfies $b_{c_1} < b_{c_2}$. The light passes through the throat into the spacetime \mathcal{M}_2 , and then returns to the spacetime \mathcal{M}_1 . Note that some additional lights from \mathcal{M}_2 will enter \mathcal{M}_1 and reach infinity in this scenario.

The impact parameters of two spacetimes satisfy [65]

$$\frac{b_1}{b_2} = \sqrt{\frac{f_2(R)}{f_1(R)}} \equiv H. \quad (9)$$

To summarize, when the impact parameter satisfies $Hb_{c_2} < b_1 < b_{c_1}$, the light enters the spacetime \mathcal{M}_1 from infinity, traverses through the throat into the spacetime \mathcal{M}_2 , returns back to \mathcal{M}_1 , and eventually exits to infinity. In our subsequent discussion, we will primarily focus on *Case 3*, as it elucidates the movement of photons that pass through the throat.

By utilizing a ray-tracing code, we can effectively determine the trajectory of light within a TSW with a Hayward profile. The light trajectory can be described by the orbit equation, denoted as Eq. (5), and can be reexpressed as follows:

$$\frac{1}{b_i^2} - \frac{f_i(r_i)}{r_i^2} = \frac{1}{r_i^4} \left(\frac{dr_i}{d\phi_i} \right)^2. \quad (10)$$

By introducing a parameter $u \equiv 1/r$, one can get

$$\Omega_i(u_i) \equiv \frac{du_i}{d\phi_i} = \sqrt{\frac{1}{b_i^2} - u_i^2 \left[1 - \frac{2M_i}{u_i^2 \left(g^3 + \frac{1}{u_i^3} \right)} \right]}. \quad (11)$$

To provide an illustration, we present in Fig. 3 the light trajectories within a TSW with a Hayward (Schwarzschild) profile, considering different values of the magnetic charge. Assuming that the light originates from the far right within spacetime \mathcal{M}_1 , we observe that smaller impact parameters result in more extensive regions of light motion within spacetime \mathcal{M}_2 . This implies that light rays with smaller impact parameters experience a greater influence from the gravitational field and exhibit more significant deflection as they traverse through the TSW.

For impact parameters $b_1 > b_{c_1}$, the inflection point of the light trajectory within spacetime \mathcal{M}_1 corresponds to the minimally positive real root of $\Omega_1(u_1)$, which we denote as u_1^{\min} . Utilizing Eq. (11), the total change of azimuthal angle within spacetime \mathcal{M}_1 can be expressed as follows:

$$\phi_1(b_1) = 2 \int_0^{u_1^{\min}} \frac{du_1}{\sqrt{\Omega_1(u_1)}}, \quad b_1 > b_{c_1}. \quad (12)$$

This situation is similar to that of the BH. When $Hb_{c_2} < b_1 < b_{c_1}$, the change in azimuthal angle (with the throat outside) in the spacetime \mathcal{M}_1 can be given as

$$\phi_1^*(b_1) = \int_0^{1/R} \frac{du_1}{\sqrt{\Omega_1(u_1)}}, \quad b_1 < b_{c_1}. \quad (13)$$

Subsequently, the light ray enters the spacetime \mathcal{M}_2 through the throat. In this region, the inflection point of the light trajectory within spacetime \mathcal{M}_2 corresponds to the largest positive real root of $\Omega_2(u_2)$, denoted as u_2^{\max} . By utilizing Eq. (11), we can calculate the change in azimuthal angle within spacetime \mathcal{M}_2 , which is given by

$$\phi_2(b_2) = 2 \int_{u_2^{\max}}^{1/R} \frac{du_2}{\sqrt{\Omega_2(u_2)}}, \quad b_2 > b_{c_2}. \quad (14)$$

4 Optical appearance of a TSW with a Hayward profile

4.1 Light rays classification

Gralla *et al.* have proposed that radiation originates from an optically and geometrically thin accretion disk situated in the equatorial plane of the BH [27]. Based on the number of times the light intersects the accretion disk and the number of light orbits ($n \equiv \phi/2\pi$), the light rays can be classified into the following categories:

- *Case 1* When $n > 1/4$, the light falls onto the front side of the disk and intersects the equatorial plane only once.
- *Case 2* When $n > 3/4$, the light penetrates through the thin disk, passing to the back side, and intersects the equatorial plane twice.

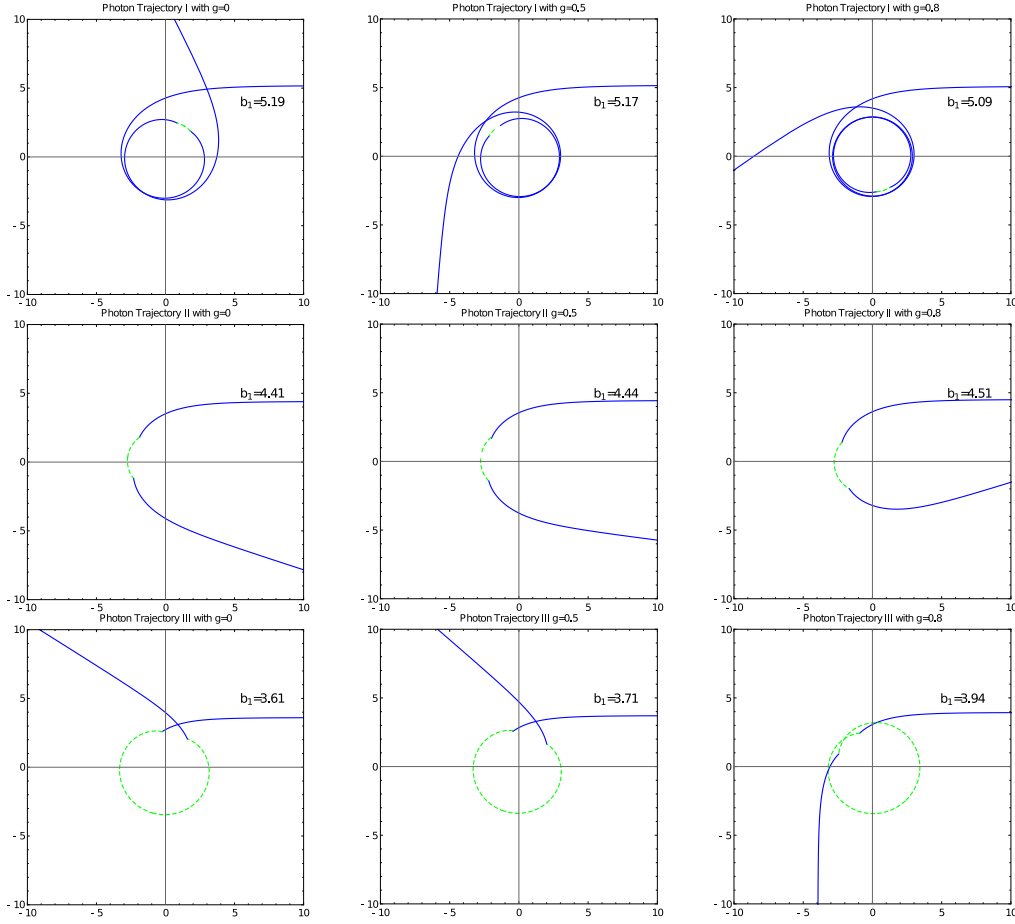


Fig. 3 Light trajectories in the polar coordinates (r, ϕ) with the impact parameters in the range $Hb_{c_2} < b_1 < b_{c_1}$. The blue curves represent the light trajectories in the spacetime \mathcal{M}_1 ($M_1 = 1$), and the green dashed curves represent the light trajectories in the spacetime \mathcal{M}_2 ($M_2 = 1.2$). *Left Panel*– magnetic charge $g = 0$ (Schwarzschild TSW scenario), *Middle Panel*– magnetic charge $g = 0.5$ and *Right Panel*– magnetic charge $g = 0.8$. We take throat radius $R = 2.6$.

- *Case 3* When $n > 5/4$, the light reaches the front side of the accretion disk once again, intersecting the equatorial plane more than three times. These additional intersections contribute to an enhanced brightness observed by an observer.

In the case of a TSW with a Hayward profile, we consider the presence of a static observer and a thin accretion disk situated in the spacetime \mathcal{M}_1 . The static observer is positioned at the north pole, while the accretion disk resides in the equatorial plane and emits radiation isotropically in the rest frame of the static worldlines. When the light enters spacetime \mathcal{M}_1 and subsequently falls into spacetime \mathcal{M}_2 through the throat, the number of orbits within the TSW can be defined as follows [66]:

$$n_1(b_1) = \frac{\phi_1(b_1)}{2\pi}, \quad (15)$$

$$n_2(b_2) = \frac{\phi_1^*(b_1) + \phi_2(b_1/H)}{2\pi}, \quad (16)$$

$$n_3(b_1) = \frac{2\phi_1^*(b_1) + \phi_2(b_1/H)}{2\pi}. \quad (17)$$

In the case where the number of orbits is n_1 , it corresponds to the scenario similar to that of a BH. If $n_2 < 3/4$ and $n_3 > 3/4$, the outgoing reflected light within spacetime \mathcal{M}_1 falls onto the back side of the accretion disk. Similarly, if $n_2 < 5/4$ and $n_3 > 5/4$, the outgoing reflected light within spacetime \mathcal{M}_1 falls onto the front side of the disk.

Figure 4 illustrates the total number of orbits as a function of the impact parameter for a TSW with a Hayward profile. It can be observed that the orbit function n_1 of the TSW with a Hayward profile closely resembles that of a Hayward BH, implying that the image seen by an observer of the TSW contains the image of the BH. However, it should be noted that additional orbit functions n_2 and n_3 appear in the TSW scenario, indicating the presence of additional ring structures in the TSW image. Moreover, it has been observed that an increase in the value of the parameter g leads to a reduction in the range of the impact parameter b compared to a TSW with a Schwarzschild profile ($g = 0$). This suggests that the additional ring structures are drawn inward towards the BH as the magnetic charge increases.

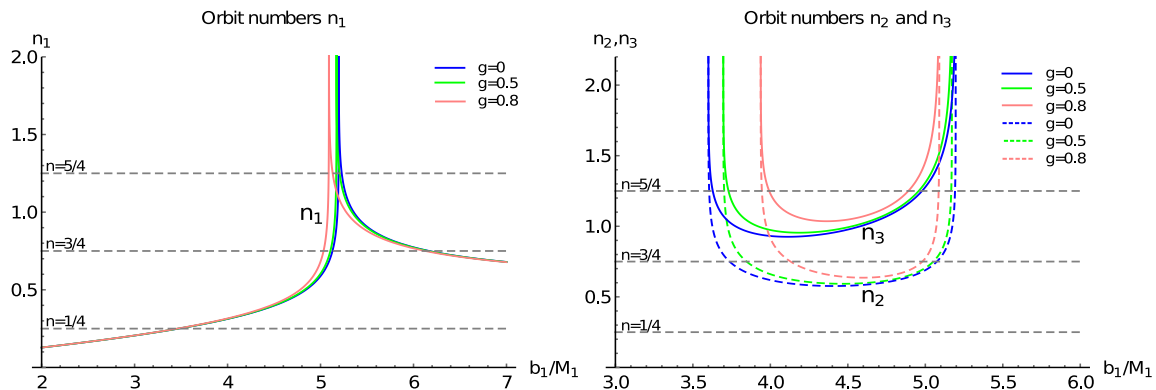


Fig. 4 Total orbit number as a function of the impact parameter for a TSW with a Hayward profile. The BHs mass are taken as $M_1 = 1$, $M_2 = 1.2$ and the throat radius is taken as $R = 2.6$. The blue, green, and pink curves represent the magnetic charges $g = 0$ (Schwarzschild TSW scenario), $g = 0.5$ and $g = 0.8$, respectively.

4.2 Observed intensity and transfer functions

As mentioned earlier, the light can gain additional brightness through multiple intersections with the accretion disk. The total observed intensity ($\text{ergs}^{-1}\text{cm}^{-2}\text{str}^{-1}\text{Hz}^{-1}$) is the sum of these intensities. According to Liouville’s theorem, $I_e/(v_e)^3$ is conserved along the direction of light propagation, where I_e is the specific intensity of the radiation and v_e is the frequency of the radiation in a static frame. An observer located at infinity receives a specific intensity I_o with a redshifted frequency $v_o \equiv \sqrt{f}v_e$. Taking into account the conservation of I/v^3 along a ray, we obtain the following relation:

$$\frac{I_o}{v_o^3} = \frac{I_e}{v_e^3}. \quad (18)$$

For a single frequency, the observed specific intensity is

$$I_o(r) = f(r)^{3/2}I_e(r). \quad (19)$$

By integrating over the whole range of received frequencies, the total observed intensity can be written as

$$\begin{aligned} I_S(r) &= \int I_o(r)d\nu_o \\ &= \int f(r)^2 I_e(r)d\nu_e = f(r)^2 I_R(r), \end{aligned} \quad (20)$$

where $I_R(r) \equiv \int I_e(r)d\nu_e$ is the total radiation intensity from the thin accretion disk. The total observed intensity is

$$I_{\text{obs}}(b) = \sum_n f(r)^2 I_R|_{r=r_n(b)}, \quad (21)$$

in which $r_n(b)$ represents the transfer function, which provides the radial coordinate of the n th intersection between the light ray with impact parameter b and the accretion disk. The slope of the transfer function, denoted as dr/db , is defined as the (de)magnification factor [27]. In the case of a BH, the first transfer function ($n = 1$) corresponds to the “direct emission” from the accretion disk, while the second ($n = 2$) and third ($n = 3$) transfer functions represent the “lensing ring” and “photon ring”, respectively.

Figure 5 showcases the transfer function $r_n(b)$ as a function of the impact parameter b for several representative magnetic charges. The black lines represent the first transfer function ($n = 1$), which closely resembles that of the Hayward BH. It can be observed that $r_1(b)$ is proportional to b and exhibits a slope of approximately 1. This indicates that the direct emission contributes the most to the total observed flux. The blue lines correspond to the second transfer function ($n = 2$). It can be seen that the curve has an irregular shape with a slightly wider range of impact parameters, connecting at the lower end of the asymptotic curve. This illustrates that the observer perceives a “lensing band” in the case of a TSW. The green lines represent the third transfer function ($n = 3$). In addition to the usual third transfer function (which appears as an almost vertical line near b_{c_1}), two new third transfer functions are present. One of them is located close to Hb_{c_2} and exhibits the same slope as the usual third transfer function. The other one is situated to the left of b_{c_1} , and its slope is smaller than the usual third transfer function but greater than the usual second transfer function. Consequently, the observer perceives a “photon ring group” in the image.

4.3 Optical appearance of a TSW with a Hayward profile

In order to study the optical appearance of a TSW with a Hayward profile, we consider two radiation functions for the thin accretion disk. It is widely recognized that the radiation emitted by accretion disks in the Universe can be approximated by a Gaussian distribution [77]. Hence, we parameterize the radiation function of the accretion disk as a Gaussian function.

Given a BH mass of 1, the radius of the innermost stable circular orbit is found to be approximately $r_{\text{ISCO}} \simeq 6$. We will consider Model I, where the inner edge of the accretion disk is located at $r = 6$, beyond which no radiation is emit-

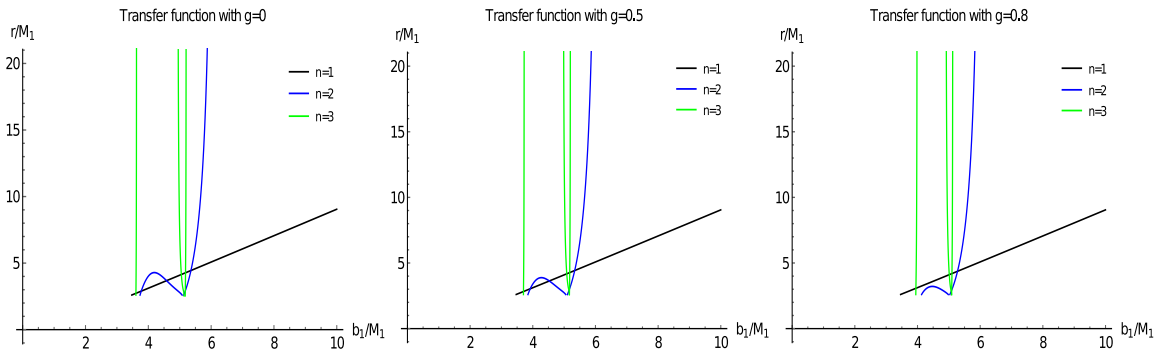


Fig. 5 Transfer functions of a TSW with a Hayward profile under the magnetic charges of $g = 0$ (Schwarzschild TSW scenario) [Panel (a)], $g = 0.5$ [Panel (b)], and $g = 0.8$ [Panel (c)]. The black, blue, and green curves are for the direct emission, lensing band, and photon ring group, respectively. The BHs mass are taken as $M_1 = 1$, $M_2 = 1.2$, and the throat radius is taken as $R = 2.6$.

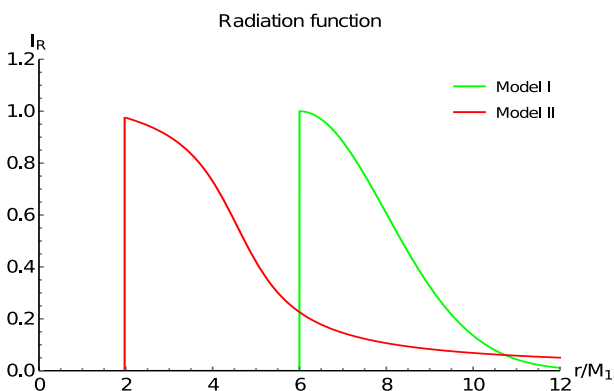


Fig. 6 The radiation intensity as a function of the radius. The green and red curves are for the Model I and Model II.

ted. To characterize the radiation function of the accretion disk, we adopt a Gaussian distribution function, which can be expressed as follows:

$$I_{R_1}(r) = \begin{cases} \exp\left[-\frac{(r-6)^2}{8}\right] & r > 6, \\ 0 & r \leq 6. \end{cases} \quad (22)$$

Next, we consider Model II, where the radiation function falls to zero more smoothly compared to Model I, in order to provide a contrast between the two models. In this case, we assume that the inner radii at which the accretion stops radiating are given by the event horizon radius of the BH ($r_+ \simeq 2$). The radiation function can be described as follows:

$$I_{R_2}(r) = \begin{cases} \frac{\frac{\pi}{2} - \arctan(r-5)}{\frac{\pi}{2} - \arctan(-3)} & r > 2, \\ 0 & r \leq 2, \end{cases} \quad (23)$$

Figure 6 presents the radiation intensity as a function of the radius for both Model I and Model II. In Model I, we display the corresponding total observed intensity I_{obs} as a function of the impact parameter b , the two-dimensional image in celestial coordinates, and the local density image in

Fig. 7. The figure clearly illustrates the distinct regions of direct emission, lensing band, and photon ring group. Taking the case of magnetic charge $g = 0.5$ (middle panel of Fig. 7), we observe that the direct emission begins at around $b \simeq 7.04M_1$ and reaches its peak at approximately $b \simeq 7.56M_1$. The maximum intensity is about 0.47. The lensing band is confined to a narrow range of $b \simeq 5.57M_1 \sim 5.83M_1$. The photon ring group appears at $b \simeq 5.17M_1$, $b \simeq 4.93M_1$, and $b \simeq 3.69M_1$. In the two-dimensional image, the boundary of the black disk corresponds to the starting position of direct emission. Within the black disk, a bright lensing band is visible, while the positions of the photon ring group progressively move towards the central region, appearing as several weaker rings. Notably, one of the new photon rings is located near Hb_{c_2} , and the other new photon ring is positioned inside the lensing band but outside b_{c_1} . It is worth mentioning that the new second transfer function is not significantly affected in this model. The top and bottom panels of Fig. 7 depict the scenarios of a TSW with a Schwarzschild profile and a TSW with a Hayward profile, both under a magnetic charge of $g = 0.8$. It is evident that an increase in the magnetic charge value causes the new photon ring to shrink inward towards the BH.

Figure 8 showcases the total observed intensity as a function of the impact parameter, the two-dimensional image, and the local density image for Model II. In this case, we can observe that the regions of direct emission, lensing band, and photon ring overlap with each other. The photon ring group in Model II mentioned in the text overlaps with the region outside the photon sphere. Let's consider the case of a magnetic charge $g = 0.5$ (middle panel of Fig. 8). The direct emission begins at approximately $b \simeq 2.85M_1$, and the photon ring group is embedded within the lensing band, forming a distinct and bright multi-layered ring structure. Notably, the lensing band consists of the usual lensing ring and an additional lensing band. The usual lensing band is confined within the range of $b \simeq 5.24M_1 \sim 5.51M_1$, while the additional lensing band is situated between Hb_{c_2} and

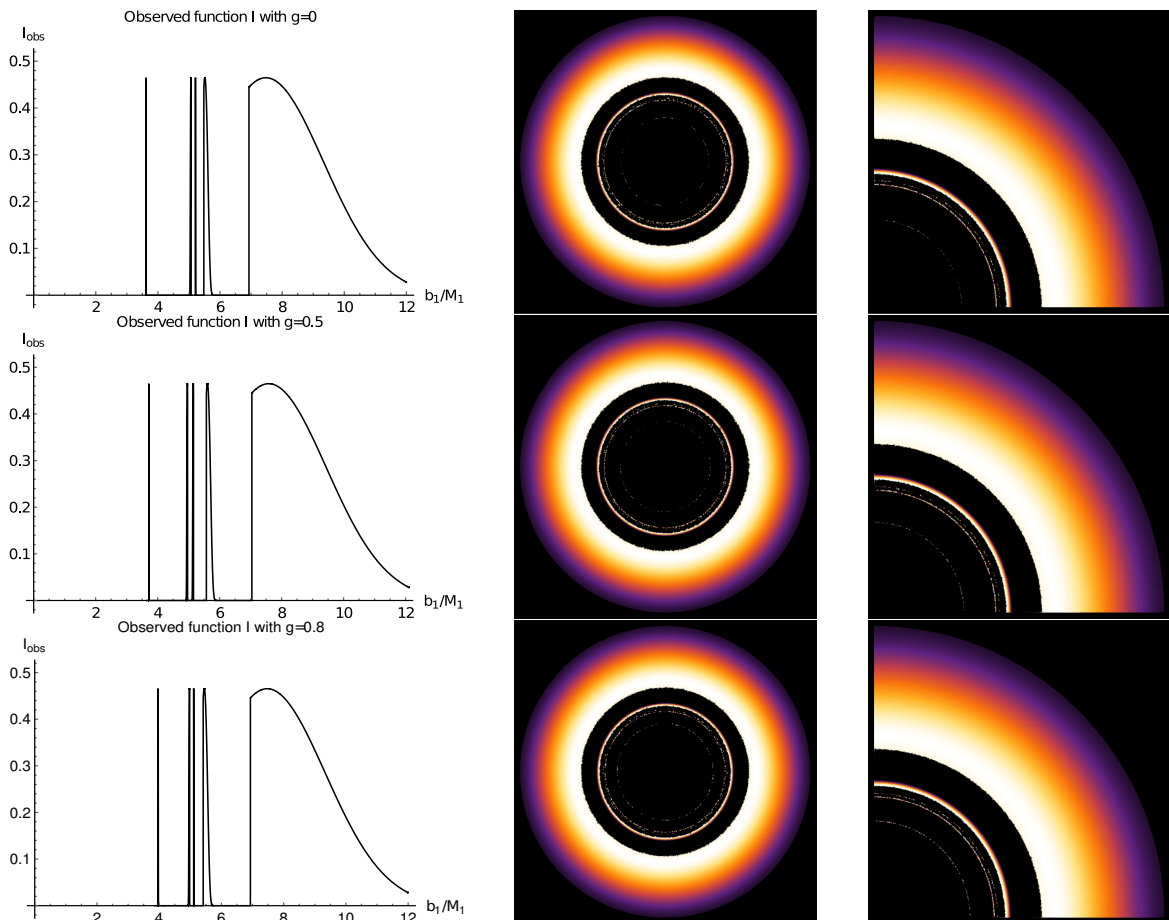


Fig. 7 Model I– The total observed intensity as a function of the impact parameter (*left panel*) for the several representative magnetic charges and the corresponding two-dimensional images (*middle panel*) together with zooming in part of the image for illustrating their local density (*right panel*). The top, middle, and bottom panels are for $g = 0$ (Schwarzschild TSW scenario), $g = 0.5$, and $g = 0.8$, respectively. The BHs mass are taken as $M_1 = 1$, $M_2 = 1.2$, and the throat radius is taken as $R = 2.6$.

b_{c_1} . This indicates that the new second transfer function contributes to the observed intensity in the case of a TSW with a Hayward profile in this radiation model.

5 Conclusions

In this analysis, we have extended the investigation of the BH shadow to the scenario of a TSW and explored the optical characteristics of a horizonless object with a Hayward profile. Through the construction of the TSW model, we obtained the effective potential of a TSW with a Hayward profile and plotted the potential function curve. The findings demonstrate that a throat connects two distinct spacetimes, and the effective potential function of the contralateral spacetime has the ability to reflect a significant portion of light back to its original spacetime.

By utilizing the null geodesic equation, we have derived a specific expression for the radial component and determined the critical impact parameter for various magnetic charges. Our findings reveal that as the magnetic charge (g)

increases, the critical impact parameter (b_{c_1}) decreases, indicating that the photon ring moves closer to the BH. Moreover, we have examined the motion of photons in a TSW with a Hayward profile. It is observed that the deflection of light can be classified into three scenarios, depending on the mass relationship between the two spacetimes. When the impact parameter satisfies $Hb_{c_2} < b_1 < b_{c_1}$, the photons enter spacetime \mathcal{M}_1 from infinity, pass through the throat to spacetime \mathcal{M}_2 , then return to spacetime \mathcal{M}_1 through the throat before finally exiting to infinity. Additionally, we have calculated the total deflection angle (ϕ) of a TSW with a Hayward profile for photons with different impact parameters.

By comparing the number of orbits between a BH and a TSW, we can analyze the behavior of photons with different total orbit numbers. Fig. 4 illustrates the variation of the total orbit number with respect to the impact parameter. It is evident that the orbit function n_1 of the TSW is equivalent to that of the BH, indicating that the image seen by an observer of the TSW contains the BH. Furthermore, the TSW

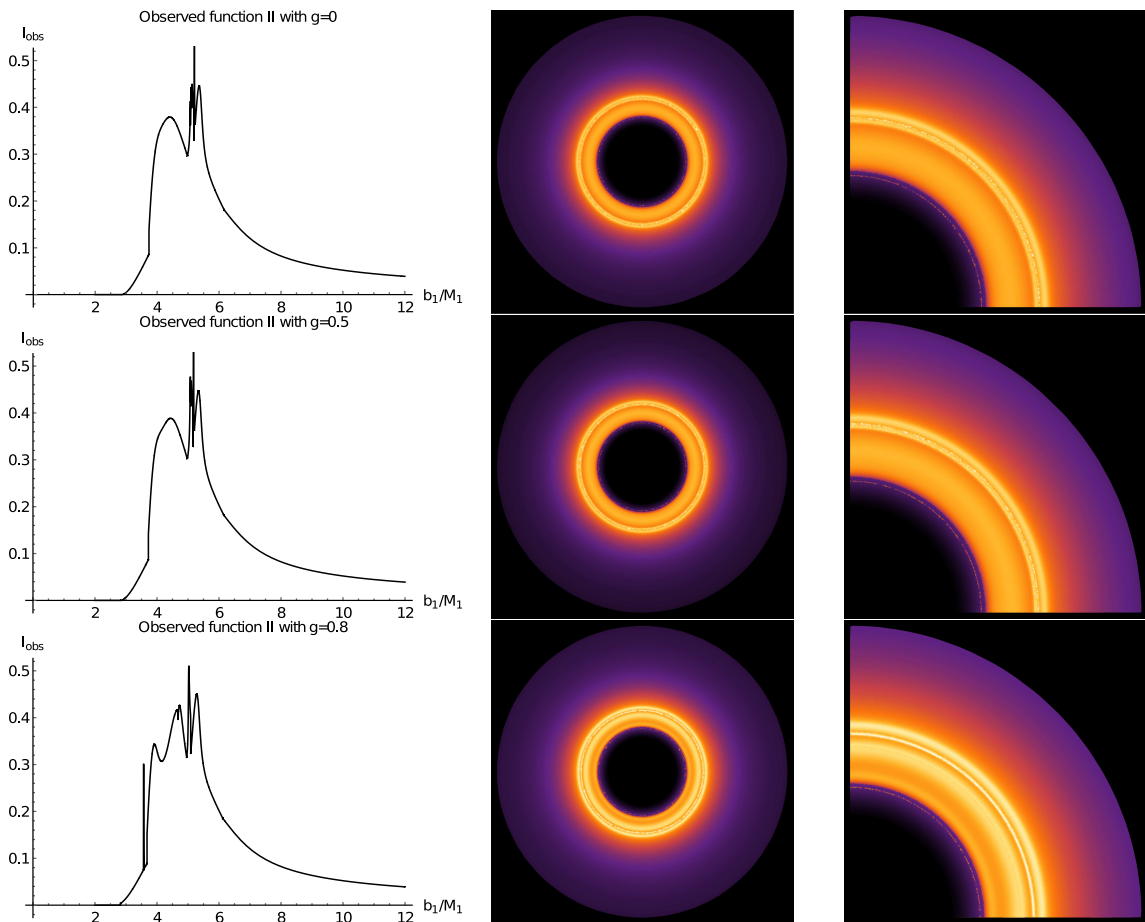


Fig. 8 Model II– The total observed intensity as a function of the impact parameter (*left panel*) for the several representative magnetic charges and the corresponding two-dimensional images (*middle panel*) together with zooming in part of the image for illustrating their local density (*right panel*). The top, middle, and bottom panels are for $g = 0$ (Schwarzschild TSW scenario), $g = 0.5$, and $g = 0.8$, respectively. The BHs mass are taken as $M_1 = 1$, $M_2 = 1.2$, and the throat radius is taken as $R = 2.6$.

situation introduces additional orbit functions n_2 and n_3 , implying the presence of additional ring structures in the TSW image. To determine the observed intensity, we investigated its relationship with the radiation intensity and performed a ray-tracing procedure to obtain the transfer function $r_n(b)$ for a TSW with a Hayward profile. Our results reveal that the first transfer function of a TSW with a Hayward profile closely resembles that of a Hayward BH. The second transfer function exhibits a monotonically increasing trend with an irregular segment preceding the monotonic part, indicating the existence of a “lensing band” in the resulting image. Additionally, in addition to the usual third transfer function of the BH, we identified two new third transfer functions in the TSW scenario, leading to the observer perceiving a “photon ring group”.

Building upon the previous discussions, we have conducted a comprehensive analysis of the optical appearance of a TSW with a Hayward profile. In order to characterize the radiation emitted by the accretion disk, we have parameterized its function using a Gaussian distribution. By con-

sidering two different Gaussian radiation models, we have investigated the observed function and the corresponding two-dimensional image. For Model I, we observed that the regions of direct emission, lensing band, and photon ring group are distinct and separated. The direct emission region starts at a specific impact parameter and reaches its peak intensity at another impact parameter. Within the black disk, a bright lensing band is clearly visible, while the photon ring group gradually moves closer to the central region, appearing as a series of weaker rings. In contrast, for Model II, the regions of direct emission, lensing band, and photon ring group overlap with each other. The photon ring group is embedded within the lensing band, forming a bright and distinctive multilayered ring structure. Notably, the lensing band consists of both the usual lensing ring and an additional lensing band. These findings highlight the potential of the optical appearance of a TSW to serve as a qualitative observational signature for the detection of wormholes in the future. By studying the distinct features and spatial arrangements of the direct emission, lensing band, and photon ring

group, researchers can potentially identify and characterize TSW in astrophysical observations.

Acknowledgments This work is supported by the National Natural Science Foundation of China (Grant No. 12133003).

References

1. J. L. Synge, The Escape of Photons from Gravitationally Intense Stars, *Mon. Not. R. Astron. Soc.* **131**: 463 (1966).
2. J. M. Bardeen, Timelike and null geodesics in the Kerr metric, In *Black holes*, p. 215-239 (1973).
3. V. Bozza, F. De Luca, G. Scarpetta, Kerr black hole lensing for generic observers in the strong deflection limit, *Phys. Rev. D.* **74**: 063001 (2006).
4. C. Bambi, K. Freese, Apparent shape of super-spinning black holes, *Phys. Rev. D.* **79**: 043002 (2009).
5. L. Amarilla, E. F. Eiroa, G. Giribet, Null geodesics and shadow of a rotating black hole in extended Chern-Simons modified gravity, *Phys. Rev. D.* **81**: 124045 (2010).
6. L. Amarilla, E. F. Eiroa, Shadow of a rotating braneworld black hole, *Phys. Rev. D.* **85**: 064019 (2012).
7. F. Atamurotov, A. Abdujabbarov, B. Ahmedov, Shadow of rotating non-Kerr black hole, *Phys. Rev. D.* **88**: 064004 (2013).
8. A. Grenzebach, V. Perlick, Claus Lämmerzahl, Photon regions and shadows of Kerr-Newman-NUT black holes with a cosmological constant, *Phys. Rev. D.* **89**: 124004 (2014).
9. V. Perlick, O. Y. Tsupko, G. S. B. Kogan, Influence of a plasma on the shadow of a spherically symmetric black hole, *Phys. Rev. D.* **92**: 104031 (2015).
10. A. A. Abdujabbarov, L. Rezzolla, B. J. Ahmedov, A coordinate-independent characterization of a black hole shadow, *Mon. Not. Roy. Astron. Soc.* **454**: 2423-2435 (2015).
11. T. Johannsen, A. E. Broderick, P. M. Plewa, et al, Testing General Relativity with the Shadow Size of Sgr A*, *Phys. Rev. Lett.* **116**: 031101 (2016).
12. A. Abdujabbarov, M. Amir, B. Ahmedov and S. G. Ghosh, Shadow of rotating regular black holes, *Phys. Rev. D.* **93**: 104004 (2016).
13. M. Sharif, S. Iftikhar, Shadow of a charged rotating Non-commutative black hole, *Eur. Phys. J. C.* **76**: 630 (2016).
14. P. V. P. Cunha, C. A. R. Herdeiro et al, Shadows of Einstein-dilaton-Gauss-Bonnet black holes, *Phys. Lett. B.* **768**: 373-379 (2017).
15. M. Z. Wang, S. B. Chen and J. L. Jing, Shadow casted by a Konoplya-Zhidenko rotating non-Kerr black hole, *JCAP.* **1710**: 051 (2017).
16. V. Perlick, O. Y. Tsupko, G. S. B. Kogan, Black hole shadow in an expanding universe with a cosmological constant, *Phys. Rev. D.* **97**: 104062 (2018).
17. R. Shaikh, P. Kocherlakota, R. Narayan, P. S. Joshi, Shadows of spherically symmetric black holes and naked singularities, *Mon. Not. Roy. Astron. Soc.* **482**: 52-64 (2019).
18. T. Zhu, Q. Wu, M. Jamil and K. Jusufi, Shadows and deflection angle of charged and slowly rotating black holes in Einstein-Æther theory, *Phys. Rev. D.* **100**: 044055 (2019).
19. S. Haroon, M. Jamil, K. Jusufi, et al, Shadow and deflection angle of rotating black holes in perfect fluid dark matter with a cosmological constant, *Phys. Rev. D.* **99**: 044015 (2019).
20. M. Y. Guo, P. C. Li, Innermost stable circular orbit and shadow of the 4D-Einstein-Gauss-Bonnet black hole, *Eur. Phys. J. C.* **80**: 588 (2020).
21. R. Kumar, S. G. Ghosh, Rotating black holes in 4D Einstein-Gauss-Bonnet gravity and its shadow, *JCAP.* **07**: 053 (2020).
22. H. C. D. Lima, Junior, L. C. B. Crispino, et al, Can different black holes cast the same shadow? *Phys. Rev. D.* **103**: 084040 (2021).
23. F. Atamurotov, K. Jusufi, M. Jamil, Axion-plasmon or magnetized plasma effect on an observable shadow and gravitational lensing of a Schwarzschild black hole, *Phys. Rev. D.* **104**: 064053 (2021).
24. Y. Meng, X. M. Kuang, Z. Y. Tang, Photon regions, shadow observables and constraints from M87* of a charged rotating black hole, *Phys. Rev. D.* **106**: 064006 (2022).
25. J. P. Luminet, Image of a spherical black hole with thin accretion disk, *Astron. Astrophys.* **75**: 228 (1979).
26. R. Narayan, M. D. Johnson and C. F. Gammie, The Shadow of a spherically accreting black hole, *Astrophys. J. Lett.* **885**: L33 (2019).
27. S. E. Gralla, D. E. Holz and R. M. Wald, Black hole shadows, photon rings, and lensing rings, *Phys. Rev. D.* **100**: 024018 (2019).
28. P. V. P. Cunha, N. A. Eiró, et al, Lensing and shadow of a black hole surrounded by a heavy accretion disk, *JCAP.* **03**: 035 (2020).
29. X. X. Zeng, H. Q. Zhang and H. B. Zhang, Shadows and photon spheres with spherical accretions in the four-dimensional Gauss-Bonnet black hole, *Eur. Phys. J. C.* **80**: 872 (2020).
30. L. Ma, H. Lv. Bounds on photon spheres and shadows of charged black holes in Einstein-Gauss-Bonnet-Maxwell gravity, *Phys. Lett. B.* **807**: 135535 (2020).

31. Q. Y. Gan, P. Wang, H. W. Wu, Photon spheres and spherical accretion image of a hairy black hole, *Phys. Rev. D.* **104**: 024003 (2021).
32. J. Peng, M. Y. Guo and X. H. Feng, Influence of quantum correction on black hole shadows, photon rings, and lensing rings, *Chin. Phys. C.* **45**: 085103 (2021).
33. G. P. Li and K. J. He, Observational appearances of a $f(R)$ global monopole black hole illuminated by various accretions, *Eur. Phys. J. C.* **81**: 1018 (2021).
34. S. Guo, K. J. He, G. R. Li and G. P. Li, The shadow and photon sphere of the charged black hole in Rastall gravity, *Class. Quant. Grav.* **38**: 165013 (2021).
35. S. Guo, G. R. Li, E. W. Liang, Observable characteristics of the charged black hole surrounded by thin disk accretion in Rastall gravity, *Class. Quant. Grav.* **39**: 135004 (2022).
36. G. Z. Guo, P. Wang, H. W. Wu, H. T. Yang, Quasinormal modes of black holes with multiple photon spheres, *JHEP.* **06**: 060 (2022).
37. K. J. He, S. C. Tan and G. P. Li, Influence of torsion charge on shadow and observation signature of black hole surrounded by various profiles of accretions, *Eur. Phys. J. C.* **82**: 81 (2022).
38. X. X. Zeng, K. J. He, G. P. Li, E. W. Liang and S. Guo, QED and accretion flow models effect on optical appearance of Euler-Heisenberg black holes, *Eur. Phys. J. C.* **82**: 764 (2022).
39. H. Falcke, F. Melia and E. Agol, Viewing the shadow of the black hole at the galactic center, *Astrophys. J. Lett.* **528**: L13 (2000).
40. K. Akiyama et al, [Event Horizon Telescope Collaboration], First *M87* Event Horizon Telescope Results. I. The Shadow of the Supermassive Black Hole, *Astrophys. J. Lett.* **L1**: 875 (2019).
41. K. Akiyama et al, [Event Horizon Telescope Collaboration], First *M87* Event Horizon Telescope Results. II. Array and Instrumentation, *Astrophys. J. Lett.* **L2**: 875, (2019).
42. K. Akiyama et al, [Event Horizon Telescope Collaboration], First *M87* Event Horizon Telescope Results. III. Data Processing and Calibration, *Astrophys. J. Lett.* **L3**: 875, (2019).
43. K. Akiyama et al, [Event Horizon Telescope Collaboration], First *M87* Event Horizon Telescope Results. IV. Imaging the Central Supermassive Black Hole, *Astrophys. J. Lett.* **L4**: 875, (2019).
44. K. Akiyama et al, [Event Horizon Telescope Collaboration], First *M87* Event Horizon Telescope Results. V. Physical Origin of the Asymmetric Ring, *Astrophys. J. Lett.* **L5**: 875, (2019).
45. K. Akiyama et al, [Event Horizon Telescope Collaboration], First *M87* Event Horizon Telescope Results. VI. The Shadow and Mass of the Central Black Hole, *Astrophys. J. Lett.* **L6**: 875, (2019).
46. K. Akiyama et al, [Event Horizon Telescope Collaboration], First Sagittarius A* Event Horizon Telescope Results. I. The Shadow of the Supermassive Black Hole in the Center of the Milky Way, *Astrophys. J. Lett.* **L12**: 930, (2022).
47. K. Akiyama et al, [Event Horizon Telescope Collaboration], First Sagittarius A* Event Horizon Telescope Results. II. EHT and Multiwavelength Observations, Data Processing, and Calibration, *Astrophys. J. Lett.* **L13**: 930, (2022).
48. K. Akiyama et al, [Event Horizon Telescope Collaboration], First Sagittarius A* Event Horizon Telescope Results. III. Imaging of the Galactic Center Supermassive Black Hole, *Astrophys. J. Lett.* **L14**: 930, (2022).
49. K. Akiyama et al, [Event Horizon Telescope Collaboration], First Sagittarius A* Event Horizon Telescope Results. IV. Variability, Morphology, and Black Hole Mass, *Astrophys. J. Lett.* **L15**: 930, (2022).
50. K. Akiyama et al, [Event Horizon Telescope Collaboration], First Sagittarius A* Event Horizon Telescope Results. V. Testing Astrophysical Models of the Galactic Center Black Hole, *Astrophys. J. Lett.* **L16**: 930, (2022).
51. K. Akiyama et al, [Event Horizon Telescope Collaboration], First Sagittarius A* Event Horizon Telescope Results. VI. Testing the Black Hole Metric, *Astrophys. J. Lett.* **L17**: 930, (2022).
52. K. Akiyama et al, [Event Horizon Telescope Collaboration], First *M87* Event Horizon Telescope Results. VII. Polarization of the Ring, *Astrophys. J.* **L12**: 910, (2021).
53. K. Akiyama et al, [Event Horizon Telescope Collaboration], First *M87* Event Horizon Telescope Results. VIII. Magnetic Field Structure near The Event Horizon, *Astrophys. J. Lett.* **L13**: 910, (2021).
54. V. Bozza, Gravitational lensing by black holes, *Gen. Relativ. Gravit.* **42**: 2269 (2010).
55. V. Cardoso, P. Pani, Tests for the existence of black holes through gravitational wave echoes, *Nat. Astron.* **1**: 586-591 (2017).
56. V. Cardoso, P. Pani, Testing the nature of dark compact objects: a status report, *Living. Rev. Relativ.* **22**: 4 (2019).
57. P. V. P. Cunha et al, Shadows of Kerr black holes with scalar hair, *Phys. Rev. Lett.* **115**: 211102 (2015).
58. P. V. P. Cunha et al, Fundamental photon orbits: black hole shadows and spacetime instabilities, *Phys. Rev. D.* **96**: 024039 (2017).
59. P. V. P. Cunha et al, Chaotic lensing around boson stars and Kerr black holes with scalar hair, *Phys. Rev. D.* **94**: 104023 (2016).

60. M. A. Bugaev et al, Gravitational lensing and wormhole shadows. *Astron. Rep.* **65**: 1185-1193 (2021).
61. S. Kasuya and M. Kobayashi, Throat effects on shadows of Kerr-like wormholes, *Phys. Rev. D.* **103**: 104050 (2021).
62. P. G. Nedkova et al, Shadow of a rotating traversable wormhole, *Phys. Rev. D.* **88**: 124019 (2013).
63. M. Visser, Traversable wormholes from surgically modified Schwarzschild space-times, *Nucl. Phys. B.* **328**: 203 (1989).
64. N. Tsukamoto, Gravitational lensing by two photon spheres in a black-bounce spacetime in strong deflection limits, *Phys. Rev. D.* **104**: 064022 (2021).
65. X. B. Wang, P. C. Li, C. Y. Zhang, M. Y. Guo, Novel shadows from the asymmetric thin-shell wormhole, *Phys. Lett. B.* **811**: 135930 (2020).
66. J. Peng, M. Y. Guo, X. H. Feng, Observational signature and additional photon rings of an asymmetric thin-shell wormhole, *Phys. Rev. D.* **104**: 124010 (2021).
67. M. Guerrero, G. J. Olmo, D. R. Garcia, D. G. S. Chillón, Light ring images of double photon spheres in black hole and wormhole spacetimes, *Phys. Rev. D.* **105**: 084057 (2022).
68. A. Eichhorn, A. Held and P. V. Johannsen, Universal signatures of singularity-resolving physics in photon rings of black holes and horizonless objects, *JCAP.* **01**: 043 (2023).
69. M. Guerrero et al, Multiring images of thin accretion disk of a regular naked compact object, *Phys. Rev. D.* **106**: 044070 (2022).
70. R. C. Rubio et al, Toward very large baseline interferometry observations of black hole structure, *Phys. Rev. D.* **106**: 084038 (2022).
71. Y. Q. Chen, P. Wang, H. W. Wu, H. T. Yang, Observational appearance of a freely-falling star in an asymmetric thin-shell wormhole, *Eur. Phys. J. C.* **83**: 361 (2023).
72. W. Javed, S. Riaz, R. C. Pantig, A. Övgün, Weak gravitational lensing in dark matter and plasma mediums for wormhole-like static aether solution, *Eur. Phys. J. C.* **82**: 1057 (2022).
73. H. Huang, J. Kunz, J. B. Yang, C. Zhang, Light ring behind wormhole throat: Geodesics, images, and shadows, *Phys. Rev. D.* **107**: 104060 (2023).
74. J. M. Bardeen, *Proc. of GR5, Tiflis, Georgia: U.S.S.R.* (1968).
75. S. A. Hayward. Formation and evaporation of nonsingular black holes, *Phys. Rev. Lett.* **96**: 031103 (2006).
76. S. Guo, G. R. Li, E. W. Liang, Influence of accretion flow and magnetic charge on the observed shadows and rings of the Hayward black hole, *Phys. Rev. D.* **105**: 023024 (2022).
77. S. N. Zhang, Black hole binaries and microquasars, *Front. Phys.* **8**: 630 (2013).